Turbulent dynamics in a two-dimensional paraxial fluid of light

Myrann Baker-Rasooli ⬤, Wei Liu ⬤, Tangui Aladjidi ⬤, Alberto Bramati ⬤, and Quentin Glorieux ⬤*

Laboratoire Kastler Brossel, Sorbonne University, CNRS, ENS-PSL University, Collège de France; 4 Place Jussieu, 75005 Paris, France

Turbulence in quantum fluids has, surprisingly, a lot in common with its classical counterpart. Recently, cold atomic gases has emerged as a well-controlled experimental platform to study turbulent dynamics. In this work, we introduce a system to study quantum turbulence in optics, with the major advantage of having access to a wide range of characterization tools available for light fields. In particular, we report the temporal dynamics of density and phase and we show the emergence of isotropy in momentum space and the presence of different scaling laws in the incompressible kinetic energy spectrum. The microscopic origin of the algebraic exponents in the energy spectrum is discussed by studying the internal structure of quantized vortices within the healing length and their clustering at larger length scales. These results are obtained using two counterstreaming fluids of light, which allows for a precise preparation of the initial state and the *in situ* measurement of the compressible and incompressible fluid velocity.

I. INTRODUCTION

In a pioneering theoretical work, Onsager made the connection between turbulence and point vortex dynamics in a two-dimensional (2D) classical fluid [1]. This model found a direct application for incompressible superfluids such as He II, where vortices are quantized and can be considered as point-like objects [2]. As a consequence, the study of quantum turbulence [3], i.e., the chaotic motion in quantum fluids such as superfluids, has largely been motivated by the expectation that understanding the dynamics of vortices in quantum fluids will help our comprehension of the general nature of turbulence. However, due to the strong interactions, a quantitative microscopic model does not exist for superfluid helium which complicates the comparison between theory and experiments [4], and ultra-cold atoms have emerged as a platform of choice to study quantum turbulence [5–8]. Atomic Bose-Einstein condensates (BECs) have allowed to observe Kelvin waves cascade [9] and vortex tangle in superfluid turbulence [10]. More recently, 2D turbulence was studied in the BEC and important phenomena have been evidenced including vortex clustering [11], direct energy cascade [12], bidirectional dynamic scaling [13], and the self-similarity dynamic [14].

In this work, we introduce a platform for studying quantum turbulence based on paraxial fluids of light in hot atomic vapors. In this system, superfluidity in two dimensions is demonstrated [15,16] and several hydrodynamical effects (including shockwaves and blast waves) are observed experimentally [17–20]. Thanks to optical wavefront-shaping and optical detection techniques this nonlinear system gives access to observables for quantum turbulence research such as the velocity field and the spectra associated with well-controlled few-vortex configurations. In this article, we present how to exploit these optical techniques to temporally resolve the 2D dynamics of turbulence in a quantum fluid of light.

The turbulence is initiated by colliding two counterstreaming fluids of light with controlled velocities and tunable densities [21] and we directly measure the fluid kinetic energy, which we decompose into compressible (linked to phononic-excitations) and incompressible (linked to vortices) parts. We first describe the emergence of isotropy in the system, even though we force it along a preferential direction. We then study the spontaneous appearance of vortices and their clustering; with their role in the appearance of power law in the kinetic energy spectrum at known length scales. As expected, we observe that the internal structure of the vortices, within the healing length, is responsible for the scaling exponent in the large momentum limit. Finally, we demonstrate that the single vortex and vortex pair spectrum follows a universal exponent as predicted in [22].

II. PARAXIAL FLUID OF LIGHT AND EMERGENCE OF ISOTROPY

A. Paraxial fluid of light

A paraxial fluid of light consists of a monochromatic laser beam propagating through a nonlinear medium. In the paraxial approximation, the propagation equation of the laser electric field envelope $\mathcal{E}$ is isomorphic to the Gross-Pitaevskii equation, describing the temporal evolution of the wave function for a weakly interacting quantum gas [23]. This reads as

$$i\frac{\partial \mathcal{E}}{\partial z}(\mathbf{r}_\perp, z) = \left[-\frac{1}{2n_0 k_0}\nabla_\perp^2 - \frac{k_0 \chi^{(3)}}{2n_0}|\mathcal{E}(\mathbf{r}_\perp, z)|^2 \right]\mathcal{E}(\mathbf{r}_\perp, z),$$

(1)

where k_0 is the wave vector, n_0 is the linear refractive index given by $n_0 = \sqrt{1 + \mathrm{Re}\,\chi^{(1)}}$, the nabla operator $\nabla_\perp$ must be understood as acting in the transverse $\mathbf{r}_\perp = (x, y)$ plane as a consequence of the paraxial approximation, and the nonlinear term is proportional to the third-order susceptibility at the laser frequency $\chi^{(3)}$ times the laser intensity. This last term
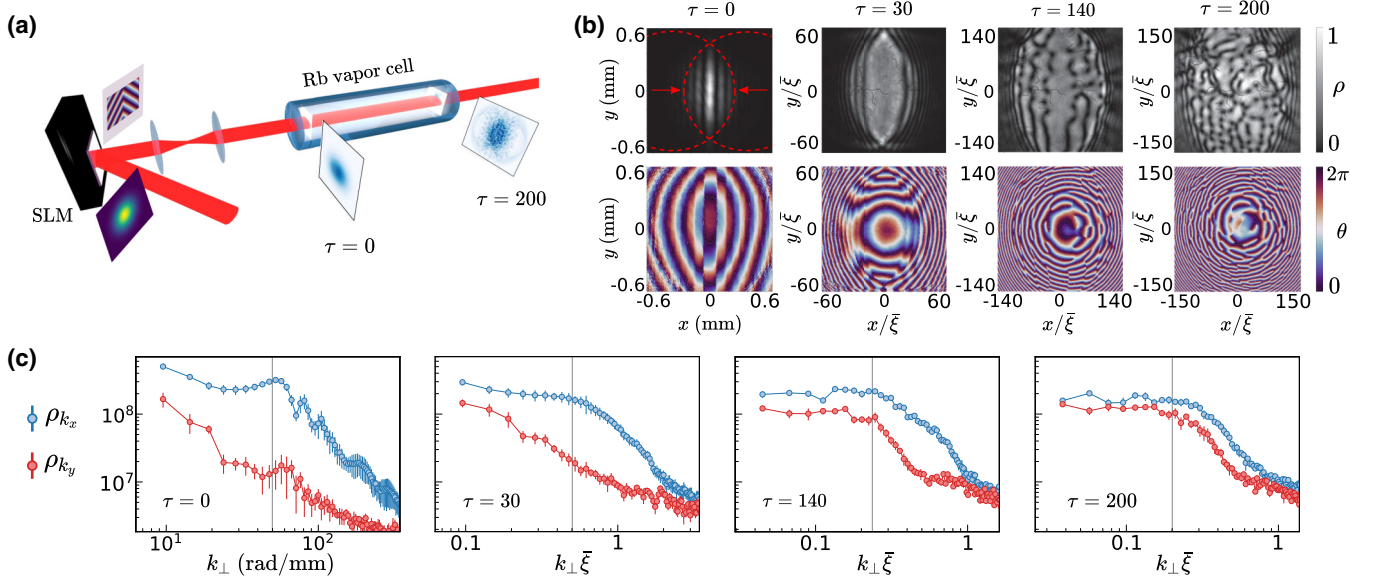
FIG. 1. Emergence of isotropy. (a) Simplified setup. A 780-nm laser beam is sent on a SLM imaged at the input of the 5-cm-long Rb vapor cell. The phase modulation leads to two counterpropagating beams in the transverse plane. The output plane of the nonlinear medium is imaged on a camera. (b) Top: Experimental images of the intensity. Bottom: Associated phase. From left to right $\tau = 0, 30, 140, 200$. (c) Averaged density spectrum along k_x (blue) and k_y (red) over 20 random realizations for different values of τ. The solid gray line represents the forcing frequency ($k_f = 2\pi \times 8$ mm^{-1}), imposed by the angle between the two fluid sets on the SLM. For all $\tau > 0$, $k_f \bar{\xi}$ is kept constant and $\bar{\xi} = 4$ μm at $\tau = 200$.

induces an effective photon-photon interaction and is set negative to ensure a stable superfluid with repulsive interactions. In this formalism, each transverse plane at fixed z, is a temporal snapshot of the evolution for an ideal 2D system.

B. Effective time and adimensional equation

The light field within the nonlinear medium is not directly accessible experimentally and the temporal evolution. We can adimension the propagation equation of the laser electric field by incorporating the fluid interaction into a new variable $\tau = L/z_{\mathrm{NL}}$, where $z_{\mathrm{NL}} = [-\frac{k_0}{2n_0}\chi^{(3)}|\mathcal{E}(\mathbf{r}_\perp, z)|^2]^{-1}$ is the characteristic nonlinear axial length and L is the length of the nonlinear medium. After rescaling the transverse quantities ($\tilde{\mathbf{r}} = \mathbf{r}/\bar{\xi}$, $\tilde{\nabla}_\perp = \bar{\xi}\nabla_\perp$) by the transverse healing length $\bar{\xi} = \sqrt{\frac{z_{\mathrm{NL}}}{k_0}}$, we obtain for $\psi = \frac{\mathcal{E}}{|\mathcal{E}|}$:

$$i\frac{\partial \psi}{\partial \tau} = \left(-\frac{1}{2}\tilde{\nabla}_\perp^2 + |\psi|^2\right)\psi. \qquad (2)$$

In this form, it becomes clear that following the evolution of the system can be done by tuning the ratio $\tau = L/z_{\mathrm{NL}}$ and, in particular, by tuning the nonlinear susceptibility $\chi^{(3)}$ [17,19].

C. Experimental description

In the experiment, we create two fluids of light by propagating a 780-nm diode laser set close to the resonance of the ^{87}Rb D2 line within a warm vapor cell of rubidium which acts as a nonlinear medium. As suggested in [21] and pictured in Fig. 1(a), we inject two counterstreaming fluids of light by imposing opposite wave vectors to the right and the left sides of the laser beam with a spatial light modulator (SLM). The angle between the wave vectors on the two sides

imposes a relative velocity to the fluids and defines the forcing spatial frequency k_f. Experimentally, we adjust k_f between $2\pi \times 8$ mm^{-1} and $2\pi \times 45$ mm^{-1} to keep the quantity $k_f\bar{\xi}$ constant while changing τ, with $\bar{\xi}$ being the mean healing length accounting for the losses during the propagation (see Appendix C).

The intensity and phase are recorded at the output of the cell ($L = 5$ cm) and typical images are shown in Fig. 1(b) (top: intensity; bottom: phase) for an increasing effective time τ. The initial state ($\tau = 0$) corresponds to the linear regime and is obtained by setting a large detuning (-5 GHz) and low laser power ($P = 10$ mW). Longer effective times ($\tau = 30, 140, 200$) are obtained by setting the detuning closer to resonance and a higher power, therefore reducing z_{NL}. Observation of the density images in Fig. 1(b) reveals the presence of instabilities which develops into pairs of vortices and antivortices with increasing τ. In this geometry with counterstreaming flows, we force the system along the x direction at short length scale, and we will first verify that turbulence develops as an anisotropic phenomenon across the system [14,24].

D. Isotropy emergence from an anisotropic forcing

In Fig. 1(c), we present the density spectrum along k_x (blue) and k_y (red) obtained by the fast Fourier transform of the density images, for different propagation times, and averaged over 20 realizations. We calibrate our spatial resolution to ensure that we resolve the inner structure of the vortices (<14 μm) (see Appendix B). For the initial state ($\tau = 0$), a clear modulation at the forcing length scale $k_f = 2\pi \times 8$ mm^{-1} is visible along k_x due to the angle imposed between the two fluids by the SLM modulation. This
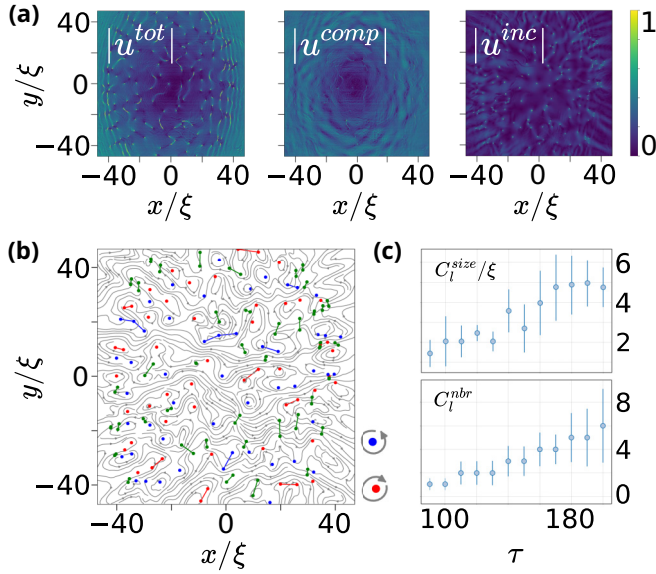
FIG. 2. Velocity decomposition and vortex clustering. (a) Modulus of each velocity field components. (b) Streamlines calculated from $\boldsymbol{u}^{\text{inc}}(\mathbf{r})$. The red and blue dots are the position of the positive and negative vortices linked by a solid line, blue or red if they belong to the same cluster, green if they belong to a dipole. (c) Average cluster number C_l^{nbr} and cluster size C_l^{size} in ξ units.

initial state reflects the anisotropic forcing at short length scale. We observe a clear reduction of the forcing peak with the increase of τ increases, but at short effective time ($\tau \leqslant 140$) the density spectrum remains anisotropic. Finally, the system evolves toward an isotropic configuration for $\tau = 200$, for which ρ_{k_x} and ρ_{k_y} overlap at all k. This observation demonstrates the emergence of statistical isotropy under anisotropic forcing, in agreement with a recent observation in ultra-cold atomic gases [14].

III. VELOCITY DECOMPOSITION AND VORTEX CLUSTERING

A. Velocity decomposition

In contrast with standard cold-atom experiments, the use of fluid of light allows for a direct access to the fluid's phase as shown in Fig. 1(b). This allows us to measure the velocity field, given by $\boldsymbol{v}^{\text{tot}}(\mathbf{r}) \propto \nabla_\perp \theta(\mathbf{r})$ (see Appendix E). To compute the kinetic energy we introduce the density-weighted velocity, given by $\boldsymbol{u}^{\text{tot}}(\mathbf{r}) = \sqrt{\rho(\mathbf{r})}\,\boldsymbol{v}^{\text{tot}}(r)$, where $\rho(\mathbf{r})$ is the light intensity. A typical example is shown in Fig. 2(a) (left) at $\tau = 200$. We then identify the compressible and incompressible parts of $\boldsymbol{u}^{\text{tot}}(\mathbf{r})$ using the Helmholtz decomposition [25,26] to separate the divergent (compressible) and rotational (incompressible) components

$$\boldsymbol{u}^{\text{tot}}(r) = \underbrace{\nabla \phi(\mathbf{r})}_{\text{compressible}} + \underbrace{\nabla \times \mathbf{A}(\mathbf{r})}_{\text{incompressible}}, \tag{3}$$

where ϕ is an arbitrary scalar and $\mathbf{A}$ an arbitrary vector field. The same decomposition can be written in the Fourier space

$$\boldsymbol{U}^{\text{tot}}(\boldsymbol{k}) = i\boldsymbol{k}\,U_\phi(\boldsymbol{k}) + i\boldsymbol{k} \times \boldsymbol{U}_A(\boldsymbol{k}), \tag{4}$$

where $U_\phi(\boldsymbol{k}) = -i\frac{\boldsymbol{k} \times \boldsymbol{U}^{\text{tot}}(\boldsymbol{k})}{\|\boldsymbol{k}\|^2}$ and $\boldsymbol{U}_A(\boldsymbol{k}) = i\frac{\boldsymbol{k} \times \boldsymbol{U}^{\text{tot}}(\boldsymbol{k})}{\|\boldsymbol{k}\|^2}$.

Thus, we write the definition of the compressible and incompressible parts in the real space

$$\nabla \phi(\boldsymbol{r}) = \text{TF}^{-1}[i\boldsymbol{k} \times U_\phi(\boldsymbol{k})],$$
$$\nabla \times \mathbf{A}(\boldsymbol{r}) = \text{TF}^{-1}[i\boldsymbol{k} \times \boldsymbol{U}_A(\boldsymbol{k})]. \tag{5}$$

The incompressible velocity is calculated by subtracting the compressible part from the total velocity $\boldsymbol{u}^{\text{inc}} = \boldsymbol{u}^{\text{tot}} - \nabla \phi(\mathbf{r})$ shown in Fig. 2(a) (right). The associated streamlines are displayed in Fig. 2(b) and overlapped with the vortex and antivortex, which are identified by the winding direction of their phase and are plotted in red and blue.

B. Vortex clustering

Using a nearest-neighbor vortex classification from [27], we sort the vortices into opposite sign dipoles (green) and the same sign clusters represented by the solid links in Fig. 2(b). The classification is then used to give quantitative elements on the clustering dynamics. In Fig. 2(c) we report the averaged cluster number C_l^{nbr} (bottom) and normalized cluster size C_l^{size}/ξ versus the propagation time τ over 20 random realizations. At short time ($\tau < 90$), no clustering mechanism is observed and only dipoles remains. By increasing τ, clustering starts occurring and C_l^{nbr} grows progressively with C_l^{size}/ξ, indicating larger scales appearing in the system. The large uncertainty is a consequence of the multiple realizations, showing that the vortex distribution strongly depends on the initial conditions.

IV. INCOMPRESSIBLE ENERGY SPECTRA

A. Kinetic energy computation

With the incompressible density-weighted velocity field, we compute the incompressible kinetic energy spectrum. The total kinetic energy is written as $E_{\text{kin}} = \frac{m}{2} \iint \rho(\boldsymbol{r})|\boldsymbol{v}^{\text{tot}}(\boldsymbol{r})|^2 dx\,dy$, with the photon mass $m = \frac{\hbar k_0}{c} \sim 10^{-36}$ kg. In the Fourier space its incompressible part can be written as

$$E_{\text{kin}}^{\text{inc}} = \frac{m}{2} \iint \left[\left|U_x^{\text{inc}}(\boldsymbol{k})\right|^2 + \left|U_y^{\text{inc}}(\boldsymbol{k})\right|^2\right] dk_x dk_y, \tag{6}$$

with $\boldsymbol{U}^{\text{inc}}_i = \text{TF}[\boldsymbol{u}_i^{\text{inc}}]$. Finally, in the turbulent regime our system tends towards a quasi-isotropic behavior. We consider the longitudinal spectrum of the incompressible kinetic energy, obtained by integrating over the azimuthal angle as

$$E_{\text{kin}}^{\text{inc}} = \frac{m}{2} k \int_0^{2\pi} \left[\left|U_x^{\text{inc}}(\boldsymbol{k})\right|^2 + \left|U_y^{\text{inc}}(\boldsymbol{k})\right|^2\right] d\Omega_k. \tag{7}$$

Thanks to the use of a SLM it is possible to shape the initial state with well-defined initial condition to measure the experimental incompressible kinetic energy spectra as presented in Fig. 3.

B. One and two vortex configurations

We first generate three simple configurations by direct imprinting with the SLM: a single vortex, a pair (same sign),
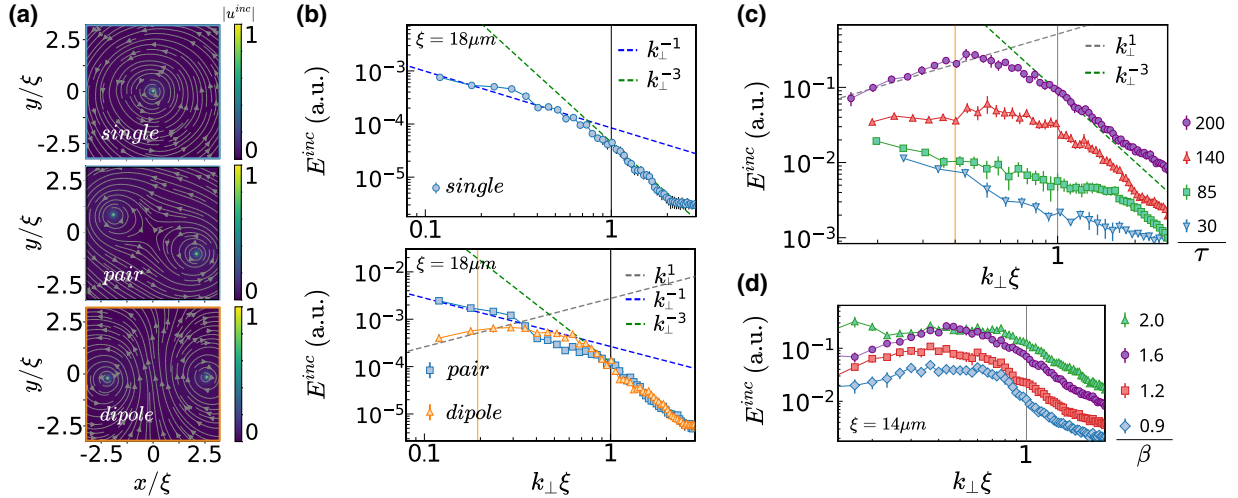
FIG. 3. Incompressible kinetic energy spectrum. (a) Streamlines and their associated $|u^{inc}|$ for a single vortex, a vortex dipole (opposite sign), and a vortex pair (same sign), from top to bottom. (b) Associated energy spectra. Those configurations are injected directly in the fluid using the SLM. Top: Blue dots correspond to a single vortex. Bottom: Orange triangles corresponds to a dipole (opposite sign) and blue squares to a pair (same sign). In both figures, dashed lines are power-law scaling with exponent -1 (blue), -3 (green), $+1$ (gray). (c) Energy spectrum for N vortices, generated with the two counterstreaming fluids, for a Mach number $\beta = v/c_s = 1.6$ and $\tau = 30, 85\ 140, 200$. The solid orange line represents the lower bound of the emerging range set at the inverse of the mean cluster radius, $1/(35\,\mu m)$, and the vertical gray line is the upper bound at 1 (fixed by the healing length at the output which is typically $14\,\mu m$ for $\tau = 200$). The gray and green dashed lines are power-law functions plotted, respectively, for k^1 and k^{-3}. (d) Spectra for different Mach numbers $\beta = 0.9, 1.2, 1.6, 2.0$ at fixed time $\tau = 200$.

and a dipole (opposite sign) and we present the experimental density and streamlines of the velocity field in Fig. 3(a). The experimental incompressible kinetic energy spectra are shown in Fig. 3(b). For a state containing only a single-vortex (and therefore no acoustic energy), the field is automatically incompressible [22]. The spectrum of a single vortex state shows a k^{-1} decay in the infrared (IR) range ($k_\perp \xi \ll 1$) which arises purely from the irrotational velocity field of a quantum vortex. The scaling is similar to point-like vortices and is the only remaining signature of the vortex far from its core. However, in contrast with the point-like model, in the ultraviolet (UV) range ($k_\perp \xi \gg 1$) we observe a k^{-3} decay which stems from the internal structure of the vortex core as described theoretically in [22,28].

As expected, the UV scaling remains identical for the pair and the dipole spectra since the vortex core structure is not modified, but the additional kinetic energy of the two-vortices state is observed throughout the spectrum in Fig. 3(b) as a vertical shift. Moreover the IR behavior differs from the isolated case. For the pair spectrum, we find a k^{-1} IR scaling similar to the single vortex configuration, which arises from the fact that we cannot distinguish the velocity field of a single vortex from a pair when we observe it far from the structure, as suggested by Fig. 3(a). On the contrary, a k^1 IR scaling is observed for the dipole configuration which originates from the cancellation of the velocity field for length scales much larger than typical intervortex separation in any neutral configuration of vortices [22].

To compare the two-vortex configuration with the single-vortex one, we calculate the ratio of the kinetic energy spectra between a pair and a single vortex as shown Fig. 4. An average factor of 2.0 ± 0.3 is observed in the region between the intervortices' distance and the healing length ξ. Moreover, we observe that, at distances below the size of the vortices,

this ratio tends towards 1, which is expected since it does not depend on the number of vortices in the system.

C. *N*-vortex configuration

Finally, we present the experimental kinetic energy spectra in the case of two counterpropagating superfluids of light in Fig. 3(c) for different propagation time τ. Interestingly, we find the same k^{-3} UV scaling (due to the vortex cores) and the same k^1 IR scaling observed for the dipole configuration (since it is also a neutral configuration). In between these two regions, a spectral range with an intermediate scaling emerges as function of τ. This range is absent at short time ($\tau = 30$) and emerges progressively with τ from the scale of the forcing frequency towards the IR. For $\tau = 200$, a fit of this intermediate range gives a $k^{-5/3}$ scaling, however, the
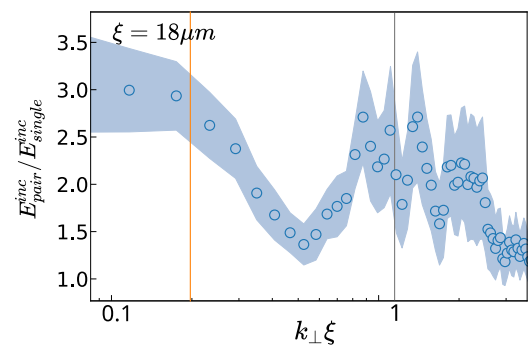

FIG. 4. Ratio of a pair of vortices with a single vortex. The average factor of 2.0 ± 0.3 is observed in the intervortex region. The orange line represents the inverse of the intervortex distance at $1/(90\,\mu m)$, and the vertical gray line is the upper bound at 1 (fixed by the healing length at the output plane).

frequency range is too narrow to conclude on the physical origin of this exponent [22,27,29–33] since, for example, accidental scaling laws were predicted in [34]. An important point is that the low-frequency cutoff of this intermediate range is given by the average cluster size as plotted in Fig. 2(c). Since this cutoff still evolves to lower frequency with τ (for $\tau = 200$), this confirms that our system has not reached the steady state yet and that a longer evolution time would allow for a broader spectral range, with potentially several decades of width.

Finally, we took advantage of the optical setup to tune the relative velocity of the counterstreaming fluids using the SLM and report it in Fig. 3(d). By tuning the fluid velocities at fixed τ for Mach numbers β (defined as the ratio between the velocity and the speed of sound) between 0.9 and 2.0, we therefore changed the forcing frequency and we verified the presence of a scaling different from -1 or -3 in the intermediate range for all these Mach numbers.

V. CONCLUSION

In this work, we evidenced and characterized turbulence in a 2D paraxial fluid of light using an anisotropic forcing. Thanks to this platform, we were able to study the phenomenon during its effective temporal evolution and observed the emergence of isotropy and scaling laws in the energy spectrum. Moreover, thanks to precise phase measurement, we had access to the velocity field and the vortex distribution and thus studied the growing clustering mechanism. By extracting the incompressible density weighed velocity, using the Helmholtz decomposition, we reported the incompressible kinetic energy spectra in several configurations. We explained different spectral regions of 1, 2, and N vortices' configurations and explored their behavior in time and for different energy injection. These results introduce a platform for studying quantum turbulence and open the way to explore acoustic waves turbulence [35–37] and more generally the out-of-equilibrium physics of quantum fluids.

APPENDIX A: EXPERIMENTAL SETUP

For creating the fluid of light, we use a 780-nm diode laser for which we can finely adjust the detuning with respect to the D2 resonance line of ^{87}Rb. A relative phase modulation of wave vector k_f between the right and left sides of the beam is imprinted using a spatial light modulator (SLM). To eliminate the unmodulated reflection on the SLM, we superpose a vertical grating to the horizontal one and select only the first vertical order in the Fourier plane with a slit. The SLM
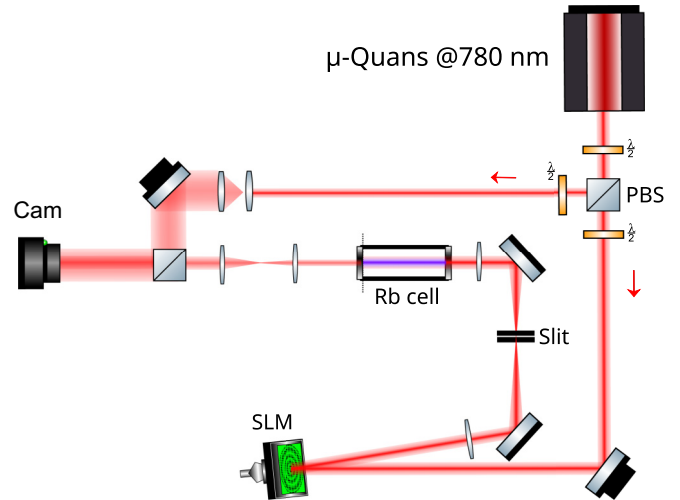

FIG. 5. Setup detail. A 780-nm laser beam is sent on a SLM imaged at the input of the 5-cm-long Rb vapor cell. The phase modulation leads to two counterpropagating beams in the transverse plane. The output plane of the nonlinear medium is imaged on a camera. A reference beam, which has been separated from the inital laser beam, is recombined with the pump before the camera for our phase measurement.

is imaged at the entrance of the nonlinear medium with a demagnification to increase the intensity of the beams. The beam waist at the medium entrance is $\omega = 0.5$ mm.

The nonlinear medium is a 5-cm rubidium cell containing a mixture of 5% of ^{87}Rb and 95% of ^{85}Rb. The output plane of the cell is imaged on a complementary metal oxide semiconductor (CMOS) camera. Using a reference beam (separate from the main beam upstream) we have access to the phase of our two counterpropagating beams by studying the interference fringes obtained after recombination before the camera. The noninteracting case ($\tau = 0$) is obtained experimentally by setting a large detuning ($\Delta = -5$ GHz) and low laser power ($P = 10$ mW). For the interacting case, the effective time τ is tuned by adjusting the laser power (up to a maximum of 500 mW) while fixing the cell temperature at 150 °C and the laser detuning at $\Delta = -2$ GHz according from the ^{85}Rb $F = 3$ to F' transition. The detailed setup is given Fig. 5.

APPENDIX B: MODULATION TRANSFER FUNCTION

We measure the modulation transfer function (MTF) and we superimpose it on our experimental spectra as shown Fig. 6. The solid line represents the cutoff frequency, showing that our imaging system does not allow us to resolve objects smaller than 3 μm.

APPENDIX C: INFLUENCE OF LOSSES AND QUANTITIES

Our nonlinear medium is not entirely described by a lossless pure $\chi^{(3)}$. Even though the general effects are not modified, the quantitative measurements provided in the main text requires to take loss into account.

To properly measure these quantities in our setup, we let a Gaussian beam propagate in the nonlinear medium and make it interfere with a reference arm on the camera. We extract
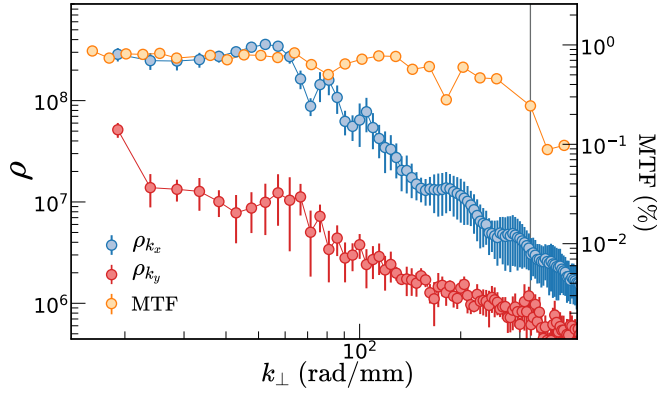
FIG. 6. MTF: Modulation transfer fFunction for different system size, overlapped over the density profile along $k_\perp$ (linear case). The 20% cutoff frequency is represented by a vertical line at 310 rad/mm.

the nonlinear accumulated phase $\Delta\theta$ along the propagation in the Rb cell. This measurement is then performed for different laser intensities (from 0 to 127 W/cm^2), as shown Fig. 7. We obtain the saturation intensity I_s as well as that of the nonlinear index n_2 by fitting the data with the solution from

$$\Delta\theta(I) = k_0 n_2 \int_0^L \frac{I(z)}{1 + \frac{I(z)}{I_s}}. \tag{C1}$$

Since the intensity in the Rb cell can be written as

$$\frac{\partial I(z)}{\partial z} = -k_0 n_2 \frac{I(z)}{1 + \frac{I(z)}{I_s}}, \tag{C2}$$

with $I(z) = I_0 e^{-\alpha z}$, α being the absorption coefficient, and equal to $78\,\mathrm{m}^{-1}$ in our case. By injecting Eq. (C2) into Eq. (C1), we obtain the nonlinear phase

$$\Delta\theta(I) = k_0 n_2 I_s \times \frac{\alpha L - \ln(1/T + I/I_s)}{\alpha}, \tag{C3}$$

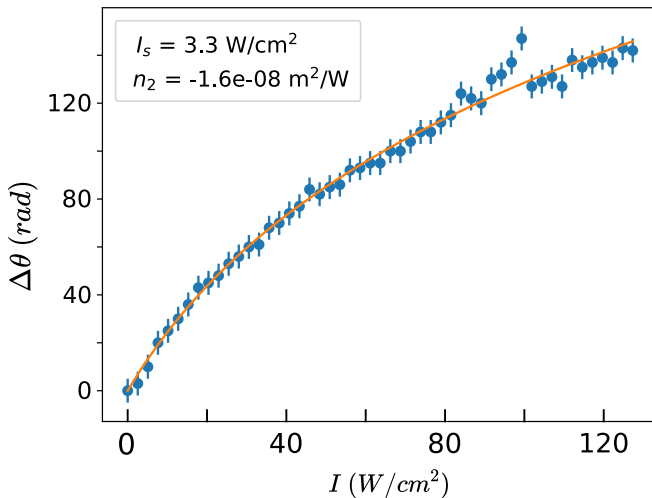with the transmission $T = e^{-\alpha L}$.

FIG. 7. Nonlinear accumulated phase along the medium. Each point is measured for a given beam intensity and the data are fitted from Eq. (C3), represented by the orange curve.
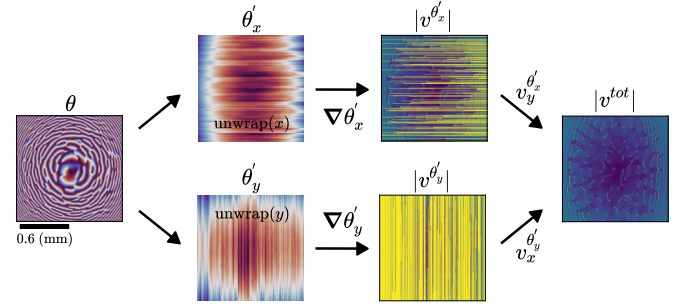

FIG. 8. Velocity computation process. The total velocity is the combination of each gradient component calculated from the 1D unwrapped phase.

The nonlinear length z_{NL} depends on the laser intensity and the medium nonlinearity. In our system both quantities are influenced by losses.

To take into account these effects and measure τ and $\bar{\bar{\xi}}$ experimentally, we define the averaged nonlinear refractive index $\bar{\Delta n} = n_2 I$ to rewrite the quantities in the form of $z_{\mathrm{NL}} = \frac{1}{k_0 \bar{\Delta n}}$ and $\bar{\bar{\xi}} = \frac{1}{k_0 \sqrt{2\bar{\Delta n}}}$.

The consequence of the losses is that the measurement of $\bar{\Delta n}$ does not allow us to know the value of the healing length ξ at the exit of the medium, but the one averaged along the Rb cell that we denote $\bar{\bar{\xi}}$. Since we know the evolution of I as function of z, we can compute the effective nonlinear refractive index Δn at the output plane of the cell by taking into account the absorption

$$\begin{aligned}
\bar{\Delta n}(L) &= \frac{1}{L} \int_0^L n_2 I(z) \mathrm{d}_z \\
&= \frac{n_2 I_0}{L} \int_0^L e^{-\alpha z} \mathrm{d}_z \\
&= \frac{n_2 I_0}{\alpha L} \times (1 - e^{-\alpha L}) \\
&= n_2 I_0 \frac{T - 1}{\ln(T)}.
\end{aligned} \tag{C4}$$

Also, we know that $\Delta n(0) = n_2 I_0$ and $\Delta n(L) = n_2 I_0 e^{-\alpha L}$. Finally, we get

$$\Delta n = \Delta n(L) = \bar{\Delta n}(L) \frac{T \ln(T)}{T - 1}. \tag{C5}$$

APPENDIX D: RECONSTRUCTION OF THE 2D VELOCITY MAP

From the phase map, we reconstruct the total velocity map, defined by $\boldsymbol{v}^{\mathrm{tot}}(\boldsymbol{r}) = \nabla\theta(\boldsymbol{r})$. To avoid any computation error on the phase we must unwrap the phase along both axes, written under the notation θ_x' and θ_y'. The total velocity is then the combination of the x and y components of each gradient, calculated from the unwrapped phase along the two axes, as shown Fig. 8.

[1] L. Onsager, Statistical hydrodynamics, Nuovo Cim. **6**, 279 (1949).

[2] J. Niemela, K. Sreenivasan, and R. Donnelly, Grid generated turbulence in helium II, J. Low Temp. Phys. **138**, 537 (2005).

[3] W. F. Vinen and J. J. Niemela, Quantum turbulence, J. Low Temp. Phys. **128**, 167 (2002).

[4] C. Nore, M. Abid, and M. E. Brachet, Kolmogorov turbulence in low-temperature superflows, Phys. Rev. Lett. **78**, 3896 (1997).

[5] S. Nazarenko and M. Onorato, Wave turbulence and vortices in Bose-Einstein condensation, Physica D **219**, 1 (2006).

[6] M. Tsubota, Quantum turbulence: From superfluid helium to atomic Bose-Einstein condensates, Contemp. Phys. **50**, 463 (2009).

[7] A. C. White, B. P. Anderson, and V. S. Bagnato, Vortices and turbulence in trapped atomic condensates, Proc. Natl. Acad. Sci. **111**, 4719 (2014).

[8] M. C. Tsatsos, P. E. Tavares, A. Cidrim, A. R. Fritsch, M. A. Caracanhas, F. E. A. dos Santos, C. F. Barenghi, and V. S. Bagnato, Quantum turbulence in trapped atomic Bose-Einstein condensates, Phys. Rep. **622**, 1 (2016).

[9] D. Kivotides, J. C. Vassilicos, D. C. Samuels, and C. F. Barenghi, Kelvin waves cascade in superfluid turbulence, Phys. Rev. Lett. **86**, 3080 (2001).

[10] E. A. L. Henn, J. A. Seman, G. Roati, K. M. F. Magalhães, and V. S. Bagnato, Emergence of turbulence in an oscillating Bose-Einstein condensate, Phys. Rev. Lett. **103**, 045301 (2009).

[11] G. Gauthier, M. T. Reeves, X. Yu, A. S. Bradley, M. A. Baker, T. A. Bell, H. Rubinsztein-Dunlop, M. J. Davis, and T. W. Neely, Giant vortex clusters in a two-dimensional quantum fluid, Science **364**, 1264 (2019).

[12] N. Navon, C. Eigen, J. Zhang, R. Lopes, A. L. Gaunt, K. Fujimoto, M. Tsubota, R. P. Smith, and Z. Hadzibabic, Synthetic dissipation and cascade fluxes in a turbulent quantum gas, Science **366**, 382 (2019).

[13] J. A. P. Glidden, C. Eigen, L. H. Dogra, T. A. Hilker, R. P. Smith, and Z. Hadzibabic, Bidirectional dynamic scaling in an isolated Bose gas far from equilibrium, Nat. Phys. **17**, 457 (2021).

[14] M. Gałka, P. Christodoulou, M. Gazo, A. Karailiev, N. Dogra, J. Schmitt, and Z. Hadzibabic, Emergence of isotropy and dynamic scaling in 2d wave turbulence in a homogeneous Bose gas, Phys. Rev. Lett. **129**, 190402 (2022).

[15] Q. Fontaine, T. Bienaimé, S. Pigeon, E. Giacobino, A. Bramati, and Q. Glorieux, Observation of the Bogoliubov dispersion relation in a fluid of light, Phys. Rev. Lett. **121**, 183604 (2018).

[16] Q. Fontaine, P.-É. Larré, G. Lerario, T. Bienaimé, S. Pigeon, D. Faccio, I. Carusotto, É. Giacobino, A. Bramati, and Q. Glorieux, Interferences between Bogoliubov excitations in superfluids of light, Phys. Rev. Res. **2**, 043297 (2020).

[17] M. Abuzarli, T. Bienaimé, E. Giacobino, A. Bramati, and Q. Glorieux, Blast waves in a paraxial fluid of light (a), Europhys. Lett. **134**, 24001 (2021).

[18] P. Azam, A. Fusaro, Q. Fontaine, J. Garnier, A. Bramati, A. Picozzi, R. Kaiser, Q. Glorieux, and T. Bienaimé, Dissipation-enhanced collapse singularity of a nonlocal fluid of light in a hot atomic vapor, Phys. Rev. A **104**, 013515 (2021).

[19] T. Bienaimé, M. Isoard, Q. Fontaine, A. Bramati, A. M. Kamchatnov, Q. Glorieux, and N. Pavloff, Quantitative analysis of shock wave dynamics in a fluid of light, Phys. Rev. Lett. **126**, 183901 (2021).

[20] P. Azam, A. Griffin, S. Nazarenko, and R. Kaiser, Vortex creation, annihilation, and nonlinear dynamics in atomic vapors, Phys. Rev. A **105**, 043510 (2022).

[21] J. D. Rodrigues, J. T. Mendonça, and H. Terças, Turbulence excitation in counterstreaming paraxial superfluids of light, Phys. Rev. A **101**, 043810 (2020).

[22] A. S. Bradley and B. P. Anderson, Energy spectra of vortex distributions in two-dimensional quantum turbulence, Phys. Rev. X **2**, 041001 (2012).

[23] I. Carusotto, Superfluid light in bulk nonlinear media, Proc. R. Soc. A: Math. Phys. Eng. Sci. **470**, 20140320 (2014).

[24] G. Falkovich, Revised universality concept in the theory of turbulence, in *Nonlinear Waves and Weak Turbulence* (Springer, New York, 1993), pp. 19–44.

[25] T.-L. Horng, C.-H. Hsueh, S.-W. Su, Y.-M. Kao, and S.-C. Gou, Two-dimensional quantum turbulence in a nonuniform Bose-Einstein condensate, Phys. Rev. A **80**, 023618 (2009).

[26] R. Panico, P. Comaron, M. Matuszewski, A. Lanotte, D. Trypogeorgos, G. Gigli, M. De Giorgi, V. Ardizzone, D. Sanvitto, and D. Ballarini, Onset of vortex clustering and inverse energy cascade in dissipative quantum fluids, Nat. Photon. **17**, 451 (2023).

[27] M. T. Reeves, T. P. Billam, B. P. Anderson, and A. S. Bradley, Inverse energy cascade in forced two-dimensional quantum turbulence, Phys. Rev. Lett. **110**, 104501 (2013).

[28] G. Krstulovic and M. Brachet, Comment on "superfluid turbulence from quantum kelvin wave to classical kolmogorov cascades," Phys. Rev. Lett. **105**, 129401 (2010).

[29] R. Numasato and M. Tsubota, Possibility of inverse energy cascade in two-dimensional quantum turbulence, J. Low Temp. Phys. **158**, 415 (2010).

[30] V. Shukla, M. Brachet, and R. Pandit, Turbulence in the two-dimensional fourier-truncated grosspitaevskii equation, New J. Phys. **15**, 113025 (2013).

[31] Y. Zhu, B. Semisalov, G. Krstulovic, and S. Nazarenko, Direct and inverse cascades in turbulent Bose-Einstein condensate, Phys. Rev. Lett. **130**, 133001 (2023).

[32] M. T. Reeves, B. P. Anderson, and A. S. Bradley, Classical and quantum regimes of two-dimensional turbulence in trapped bose-einstein condensates, Phys. Rev. A **86**, 053621 (2012).

[33] T. Simula, M. J. Davis, and K. Helmerson, Emergence of order from turbulence in an isolated planar superfluid, Phys. Rev. Lett. **113**, 165302 (2014).

[34] T. P. Billam, M. T. Reeves, and A. S. Bradley, Spectral energy transport in two-dimensional quantum vortex dynamics, Phys. Rev. A **91**, 023615 (2015).

[35] J. Skipp, V. L'vov, and S. Nazarenko, Wave turbulence in self-gravitating Bose gases and nonlocal nonlinear optics, Phys. Rev. A **102**, 043318 (2020).

[36] Y. Zhu, B. Semisalov, G. Krstulovic, and S. Nazarenko, Testing wave turbulence theory for the Gross-Pitaevskii system, Phys. Rev. E **106**, 014205 (2022).

[37] A. Griffin, G. Krstulovic, V. S. L'vov, and S. Nazarenko, Energy spectrum of two-dimensional acoustic turbulence, Phys. Rev. Lett. **128**, 224501 (2022).